nature communications

Article

https://doi.org/10.1038/s41467-025-58955-4

Shifts in MJO behavior enhance predictability of subseasonal precipitation whiplashes

Received: 23 September 2024

Accepted: 8 April 2025

Published online: 28 April 2025

Check for updates

Tat Fan Cheng[1,2,3], Bin Wang[2,4] ✉, Fei Liu[5,6,7] ✉, Guosen Chen[8] & Mengqian Lu[1,3]

Subseasonal precipitation whiplashes, marked by sudden shifts between dry and wet extremes, can disrupt ecosystems and human well-being. Predicting these events two to six weeks in advance is crucial for disaster management. Here, we show that the propagation diversity of the Madden-Julian Oscillation (MJO)—a key source of subseasonal predictability—will alter under anthropogenic warming. This is evidenced by a 40% increase in fast-propagating events by the late 21st century. Fast-propagating MJOs may rise in a period as early as 2028–2063, increasing the global risk of precipitation whiplashes through teleconnections. We propose a heuristic framework diagnosing that MJO's acceleration is primarily driven by enhanced atmospheric stabilization and El Niño-like sea surface warming. The expected rise in fast-propagating MJOs could improve the predictability of subseasonal weather whiplashes, offering critical lead time for disaster preparedness. Understanding these impending shifts is essential for enhancing subseasonal prediction capabilities.

The Madden-Julian Oscillation (MJO)[1,2] is an eastward-propagating, planetary-scale disturbance that dominates tropical intraseasonal variability during the boreal winter[3,4]. Through tropical–extratropical teleconnections[5], different phases and propagation types of the MJO have profound impacts on global rainfall patterns[6,7], extreme precipitation occurrence[8], tropical cyclone genesis[9], monsoon circulations[10,11], mid-latitude weather patterns[12–14], atmospheric rivers[15,16], Arctic amplification[17], the El Niño-Southern Oscillation[18,19], marine food chain[20], and waterborne disease[21]. We will show that a fast-propagating MJO event would be considered perilous as it triggers extreme weather whiplash, such as precipitation whiplash[22–26], and shortens the response time for hazard adaptation. Understanding the impending changes in MJO behavior is crucial for improving subseasonal-to-seasonal (S2S) forecasts and for timely decision-making in climate adaptations and agricultural and infrastructure planning[27,28].

As a complex system governed by multiple factors, the future response of MJO to anthropogenic greenhouse gas (GHG) warming remains at the forefront of research. While the numerical experiments being performed differ, existing studies concluded that anthropogenic warming could shorten periodicity and zonal wavenumber, yielding a faster eastward propagation of the MJO[29–36]. However, the physical mechanism responsible for such an acceleration remains controversial[33]. Some stressed the role of enhanced low-level convergence and vertical moisture gradient east of the MJO in accelerating its propagation[30,31,37,38], reasoning that an increased dry static stability would slow down the MJO by reducing vertical motions that would lead to weakened divergent flows[39]. Yet, theoretical studies predicted that increased dry static stability would instead accelerate the convectively coupled Kelvin wave speed, which is potentially favorable for the MJO's eastward propagation[40–42]. Warming can invigorate the MJO's convective center by increasing the water-vapor-holding

[1]Department of Civil and Environmental Engineering, The Hong Kong University of Science and Technology, Hong Kong, China. [2]International Pacific Research Center, University of Hawai'i at Mānoa, Honolulu, HI, USA. [3]Otto Poon Centre for Climate Resilience and Sustainability, The Hong Kong University of Science and Technology, Hong Kong, China. [4]Department of Atmospheric Sciences, University of Hawai'i at Mānoa, Honolulu, HI, USA. [5]School of Atmospheric Sciences, Sun Yat-Sen University, Zhuhai, China. [6]Key Laboratory of Tropical Atmosphere-Ocean System Ministry of Education, Zhuhai, China. [7]Southern Marine Science and Engineering Guangdong Laboratory, Zhuhai, China. [8]Earth System Modeling Center, Key Laboratory of Meteorological Disaster of Ministry of Education, Collaborative Innovation Center on Forecast and Evaluation of Meteorological Disasters, Nanjing University of Information Science and Technology, Nanjing, China. ✉e-mail: wangbin@hawaii.edu; Liufei26@mail.sysu.edu.cn

capacity of the atmosphere following the Clausius-Clapeyron relation[43]. Meanwhile, it decelerates the moist gravity wave (GW) speed by wave dynamics[40,44,45], which could eventually slow down the propagation of the MJO. To date, no study has quantitatively addressed the paradox of the differing roles of dry static stability and specific humidity in the future propagation speed of the MJO. Further, as far as climate resilience is concerned, our understanding of how the future MJO will shape the global distribution of compound dry and wet extremes and impact subseasonal climate predictability remains unclear.

To thoroughly understand the projected changes in the MJO requires a complete realization of its complex propagation behavior. Previous research noticed the existence of propagating and non-propagating MJO events[46,47], with the latter failing to propagate through the Maritime Continent[48,49]. With the help of unsupervised k-means clustering, a recent study unfolded four outstanding MJO archetypes, including the standing, jumping, slow, and fast modes[50], opening the door to an advanced understanding of the MJO's complex propagation. Among the prevailing MJO theories, one school of thought regards the MJO as a dynamic moisture mode driven by both the moisture and dynamic feedbacks[42,50–57]. In contrast to the moisture-mode theory, which emphasizes the moisture and cloud radiation feedbacks[58–60], the dynamic-moisture-mode theory takes into account also the wave dynamics and the boundary layer convergence feedback in a trio-interaction framework[42,50,55–57,61], which were shown to explain the MJO's westward-tilted, coupled Kelvin-Rossby wave structure by observations[62–67]. Through this framework, the origin of the diversified MJO behavior can be boiled down to two fundamental factors: the Kelvin-Rossby wave coupling strength and its structural asymmetry[42,50,55–57,61]. A tight coupling between the Kelvin wave response and the MJO's major convection gives rise to a leading boundary layer moisture convergence (BLMC) and, thereby, the propagating modes. The structural asymmetry in the MJO's coupled Kelvin-Rossby wave packet determines the slow and fast modes. The standing mode springs from a weak wave coupling that prevents a systematic eastward propagation, while the jumping mode is shaped by a strong, westward-propagating equatorial Rossby wave that hinders the MJO's eastward propagation but initiates subsequent convection over the western Pacific Ocean[68,69].

Here, we adopt the concept of MJO diversity to analyze the future changes in the MJO's diverse propagation modes and their impacts and teleconnections—aspects that were overlooked in conventional climate projection research. This analysis is based on 28 coupled general circulation models (CGCMs) participating in the sixth phase of the Coupled Model Intercomparison Project (CMIP6) under both mitigated (SSP2-4.5) and high-end (SSP5-8.5) shared socioeconomic pathways[70]. We seek to resolve the longstanding puzzle of the MJO's future eastward acceleration by proposing a heuristic diagnostic of moist GW. This diagnostic demystifies the contrasting roles of atmospheric moisture and stability in the projected change in the MJO's behavior in a systematic and quantitative manner. Notably, a recent report reveals a 31–66% increase in global subseasonal precipitation whiplashes since the mid-20th century[71]. This trend, exemplified by the 2022 severe drought and wildfire in California followed by record-breaking precipitation, suggests that the Earth's hydroclimate variability has unusually intensified under climate change. Therefore, it is imperative to understand how future MJO diversity will influence the occurrence of global subseasonal precipitation whiplash and the medium-range prediction skills under ongoing global warming, as discussed in the following sections.

Results

Performance of CMIP6 models on historical MJO diversity

We evaluate the performance of 28 CMIP6 models in simulating the four MJO archetypes. To classify the MJO archetypes in the model, we first match the simulated MJO propagation patterns from the historical experiment over 1979–2014 to the most similar benchmark archetype from observation (see Methods). Model performance is then assessed by measuring their distances to all four benchmark propagation patterns combined together (Supplementary Fig. 1a). Here, we identify the 12 best models that realistically reproduced the historical MJO diversity with a normalized root-mean-square-error (RMSE) lower than 0.3 (Supplementary Fig. 1b). Sensitivity tests are performed based on different choices of the threshold when determining good models. The different choices reveal similar results of the future change of MJO diversity (Supplementary Fig. 2). Further, we confirm that the top-performing models based on individual MJO type are among the 12 good models using the original evaluation scheme (which is based on all four MJO types combined), and likewise for the poor models (Supplementary Fig. 3). These demonstrate the aptness of the model evaluation scheme adopted herein.

The multi-model ensemble mean (MME) of the 12 good models (MME12) closely resembles the overall benchmark patterns in terms of the convective intensity, the magnitude and the extent of accompanied subsidence, as well as the phase speed based on different MJO archetypes (Supplementary Fig. 4a–j). Though the model simulations were not perfect, the successful reproduction of the four propagation archetypes supports the effectiveness of the good models in accurately simulating MJO diversity. In contrast, the poor models (those with a normalized RMSE greater than 0.6) evidently fail to reproduce the overall propagation pattern, as well as the jumping and fast-propagating archetypes (Supplementary Fig. 4k–o). A common bias observed in both good and poor models is the over-simulation of standing and jumping cases with fewer propagating cases than observations. This bias is significantly more pronounced in the poor models, suggesting an intrinsic deficiency in their ability to simulate long-propagating MJO events adequately. The sources of model deficiencies in reproducing the MJO propagation diversity could stem from the inadequately simulated equatorial Kelvin-Rossby wave couplet[61,72], an overly simulated effect of the Maritime Continent barrier[48,49,73], and mean state bias[74–76]. Given the relatively accurate representation of MJO propagation archetypes and event frequencies by the 12 good models, the subsequent analyses are based on their MME.

Increased frequency of intense fast and jumping MJOs

The good models almost unanimously predict a burgeoning trend of more jumping and fast-propagating MJO events in future climates. Over the same 35 boreal winter seasons (November–April), the number of the fast-propagating MJO events is projected to increase significantly by about 40% on average during the far-future period (2064–2099) compared to the historical period (Fig. 1a, b). The stationary and slow-moving events will be slightly fewer or unchanged. Alongside the growth of fast-moving events, jumping MJO will increase by about 23%, with a notable propagation pattern transformation into a more eastward-propagating type. The signal of an increased frequency of fast-propagating and jumping MJO events is expected to emerge as early as 2028 to 2063, contributing to an overall rise in the total number of future MJO events under both mitigated and high-end scenarios. On convection extent, future warmer climates will witness a zonal expansion of the MJO convection (more to the east), which deepens as it travels eastward (Supplementary Fig. 5). On propagation speed, the lead-lag correlation analysis and the event-based composite analysis both show an overall acceleration of the MJO propagation speed by 17–20%. The upward trend of long- and fast-propagating cases indicates that the Maritime Continent barrier[48,49,73] will become less insurmountable for the MJO as the climate warms.

Future MJO is poised to induce stronger downpours, with the overall associated rain rate projected to increase significantly by about 38% (Supplementary Fig. 5e). Categorizing the MJO events by their

propagation archetypes yields several important insights. Firstly, fast-propagating events produce the most significant rainfall accumulation among all archetypes in both past and future climates due to their long and persistent excursion (Fig. 2). Under the high-emission scenario, a fast-moving MJO event will, on average, produce a tropical mean (10°S–10°N) 20–70-day rainfall accumulation anomaly as high as 1804 mm (Fig. 2k). The greatest increase in rainfall occurs as the fast-moving MJO reaches the western Pacific warm pool (Fig. 2l). Secondly, whilst all types of MJO events are projected to accompany a greater rainfall intensity, the greatest uptick (+419 mm or +45%) in the resultant rainfall accumulation is found in future jumping events (Fig. 2e), followed by fast-propagating events (+329 mm or +22%) (Fig. 2k). Considering the projected increase in their occurrence as the climate warms, the gross hydrological impacts of fast-propagating and jumping MJO events are anticipated to be unprecedentedly severe. Thirdly, the MJO's future jumping behavior will transform into an eastward propagation. This transformation results from intensified lower-level moistening and condensational heating across the EIO and the equatorial western Pacific (Supplementary Figs. 5f, 6d), promoting deep convection and closing the propagation gap between the two centers of convection (Fig. 2e). This burgeoning jumping pattern, plus the higher traveling speed of fast-propagating events, constitutes the overall eastward acceleration of the MJO.

Role of the altering MJO diversity in global subseasonal precipitation whiplashes

More frequent fast and jumping MJO events are expected to trigger disruptive weather fluctuations worldwide. One important paradigm in this regard is precipitation whiplash[22–26], characterized by rapid swings between wet and dry extremes. By identifying the subseasonal precipitation whiplash associated with the MJO (see Methods), we construct a global map showing the difference in precipitation whiplash occurrence between fast/jumping and slow/standing cases, normalized by the frequency of each MJO archetype (Fig. 3). Compared to the historical run, the future high-emission scenario will witness a substantially greater risk of precipitation whiplash occurrence heralded by increasing fast and jumping MJOs under climate change (Fig. 3a, b). The response of the precipitation whiplash occurrence between the historical and future warmer climates is considerably consistent, evidenced by a pattern correlation coefficient of 0.68. Hotspots of increased precipitation whiplash occurrence are expected to take place in central Africa, the Middle East, Central Asia, East Asia (or more specifically, the lower reaches of the Yangtze River basin), the Maritime Continent, equatorial Pacific Ocean, the northern Amazon rainforest, East Coast of the continental United States, coastal Argentina, South Atlantic Ocean, and West Antarctica. These precipitation whiplash hotspots, particularly those on land, can result in various forms of cascading hazards[26] that pose unprecedented stress to ecosystem services, existing infrastructure, water and food security, and human safety.

The rise in global subseasonal precipitation whiplash can be explained by the disparate teleconnection patterns across the MJO archetypes[14,28]. In contrast to the slow and standing ones, fast and jumping cases typically link to stronger poleward-propagating Rossby wave trains[77] into the mid-latitudes in both hemispheres, as indicated by the 500-hPa streamfunction variability difference (Fig. 3a). Global warming is expected to amplify such a difference in Rossby wave responses, particularly in the northern hemisphere. The increased subseasonal precipitation whiplashes in extratropical regions, including East Asia, the East Coast of the continental United States, and Central Asia, juxtapose with the enhanced circulation variability (Fig. 3b). Even with a weaker change over the tropics and West Antarctica, the increased 500-hPa streamfunction variability still elucidates the heightened risk of precipitation whiplash there. With the expected rise in fast and jumping events (Fig. 1), the risk of global precipitation whiplash is anticipated to significantly intensify (Supplementary Fig. 7). The findings underscore the collective role of anthropogenic warming and the fast-propagating and jumping MJO teleconnection in amplifying global risks of compound hazards. The widening contrast in global teleconnection of compound hazard risks across the archetypes will likely be missing in conventional MJO analysis that disregards propagation types.

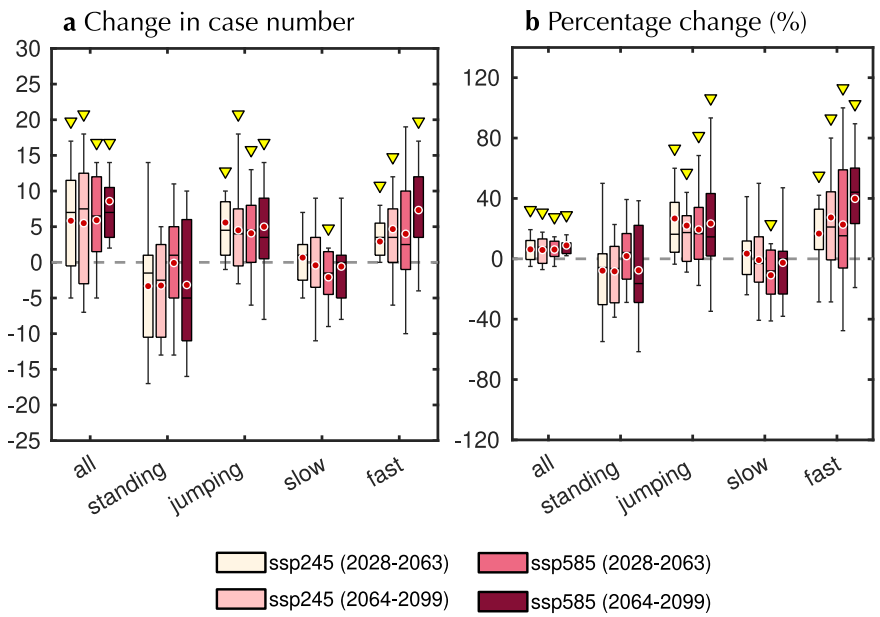

Fig. 1 | The preferred Madden-Julian Oscillation (MJO) propagation archetypes in future climate scenarios. a Boxplots of changes in the number of events for each MJO archetype in the near- (2028–2063) and far-future (2064–2099) under the SSP2-4.5 and SSP5-8.5 scenarios compared to the historical period (1979–2014) based on the 12 good models. **b** Similar to panel a, but for relative percentage changes (%). Bars of a boxplot from bottom to top refer to the minimum, the lower (25th) quartile, the median, the upper (75th) quartile, and the maximum. Red dots denote the sample means. The yellow downward-pointing triangles indicate that the sample means significantly differ from zero at the 0.1 level (Student's *t* test).

https://doi.org/10.1038/s41467-025-58955-4

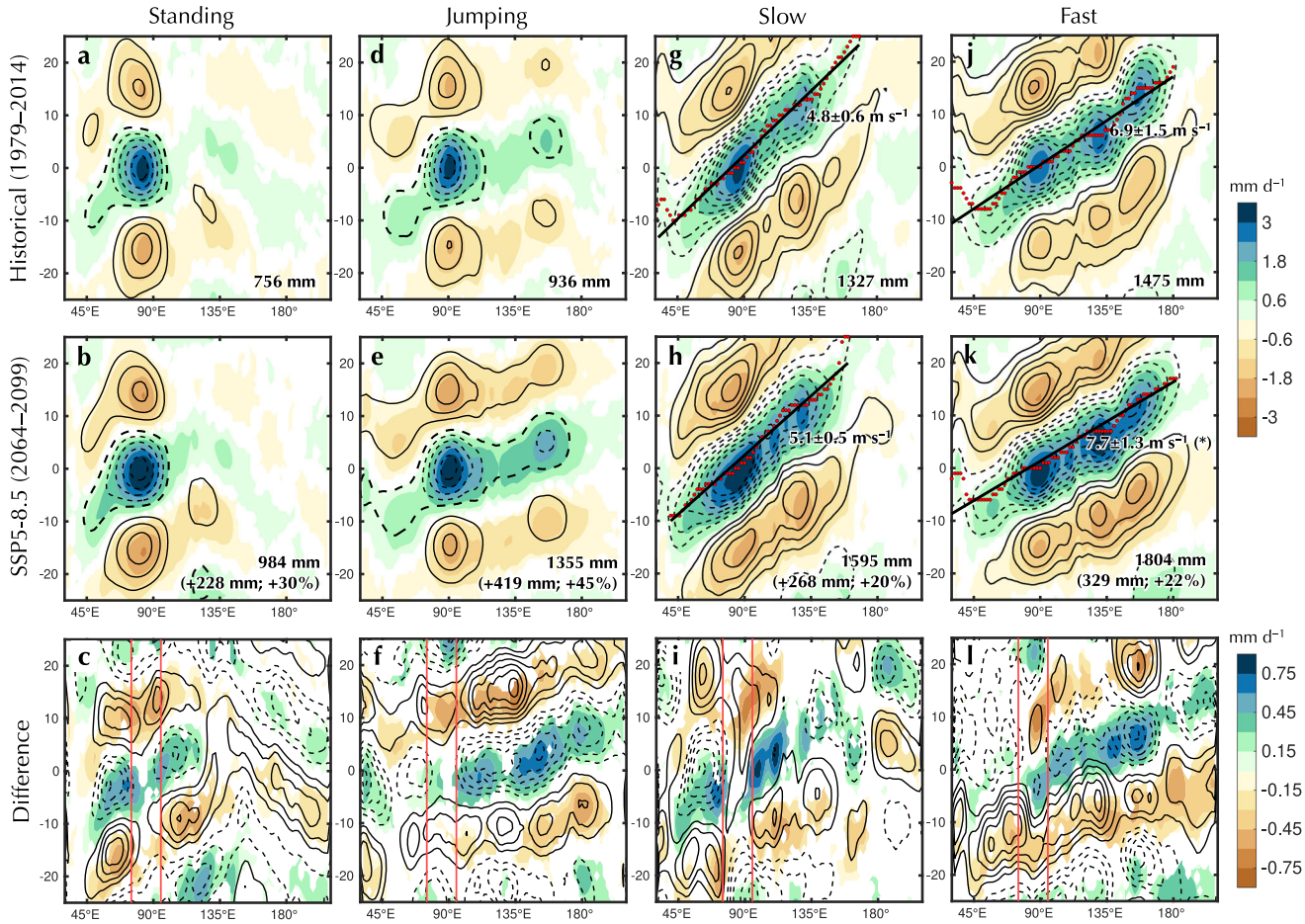

Fig. 2 | Future changes in different archetypes of Madden-Julian Oscillation (MJO) propagation and the associated rainfall. Hovmöller diagrams of the mean equatorial (10°S–10°N) 20–70-day rainfall anomaly (shading, units: mm day^{-1}) and the outgoing longwave radiation (OLR) anomaly (contour, interval: 5 W m^{-1}) averaged over all the standing MJO events in the (**a**) historical (1979–2014) and **b** far-future (2064–2099) SSP5–8.5 scenarios based on the multi-model ensemble mean of the 12 good models (MME12). **c** The difference between the two scenarios, with the shading showing the values with the sign agreed by ≥ 66% of the models. Dashed contours denote negative values, while solid ones denote positive values. The bottom right shows the tropical mean total 20–70-day rainfall accumulation associated with the MJO events. **d**–**l** Similar to panels **a**–**c**, but for **d**–**f**, jumping, **g**–**i**, slow, **j**–**l**, and fast events. The phase speed, with the uncertainty showing inter-model spread (±1 S.D.), is estimated using the regression approach (see Methods).

The physical origin of the MJO acceleration under anthropogenic warming

A classic conundrum remains unresolved: Why does the MJO accelerate with anthropogenic GHG warming? Observational and theoretical evidence have demonstrated that a standing MJO convective complex is characterized by a vertical alignment of convection and moist static energy (MSE) without a tilt of ascending motion and MSE (or equivalent potential temperature)[61,72,78]. In contrast, an eastward propagating MJO complex is characterized by a rearward tilt of ascending motion and MSE led by the BLMC ahead of the MJO convection. The trio-interaction theory[57] suggests that the MJO propagation is closely tied to pre-existing BLMC that accumulates MSE, generates convective instability, couples the convective heating and the equatorial Kelvin-Rossby wave packet, and eventually propels the convective core eastward. In the following, we will elucidate the collective role of atmospheric and oceanic forcings in shaping the strength and asymmetry of the Kelvin-Rossby wave couplet, shedding light on the physical origin of the MJO's future eastward acceleration.

Regarding atmospheric forcings, GHG warming accelerates the moist gravity (or Kelvin) wave speed and deepens the skewness of the Kelvin-Rossby wave packet structure. The good models simulate an iconic Matsuno-Gill response of the atmosphere to the MJO's diabatic heating, as manifested in an equatorial trough of Kelvin wave response east of the MJO convection and two off-equatorial lows of the Rossby wave response to the west[79,80] (Fig. 4a). Of particular interest is a stronger Kelvin wave response with enhanced convectively coupled easterlies during future MJO events (Fig. 4b, c). The MJO is closely coupled with moist, long Rossby and Kelvin waves, forming a wave structure less skewed than the Gill pattern[57,80]. A shape parameter for this pattern is the Rossby-Kelvin (R-K) ratio[42,57,61], which is defined as the ratio of the equatorial (10°S–10°N) Rossby wave westerly averaging over 40° to the west of the MJO convection and the Kelvin wave easterly averaging over 120° east of it.

The R-K ratio describes the relative strength of the Rossby and Kelvin wave components in the structure of the MJO. The R-K ratio describes the relative strength of the Rossby and Kelvin wave components in the structure of the MJO. A higher R-K ratio suggests the Rossby wave is more dominant, while a lower ratio indicates a greater contribution from the Kelvin wave. This ratio affects how the MJO moves: the Rossby wave, excited by MJO heating, tends to push the MJO complex westward, whereas the Kelvin wave component drives it eastward. The Kelvin wave component is a low-pressure system located to the east of MJO convection[57]. A stronger Kelvin wave component enhances boundary layer moisture convergence, which boosts MSE, atmospheric convective instability, and shallow convection east of the MJO convection, thereby promoting its eastward movement.

https://doi.org/10.1038/s41467-025-58955-4

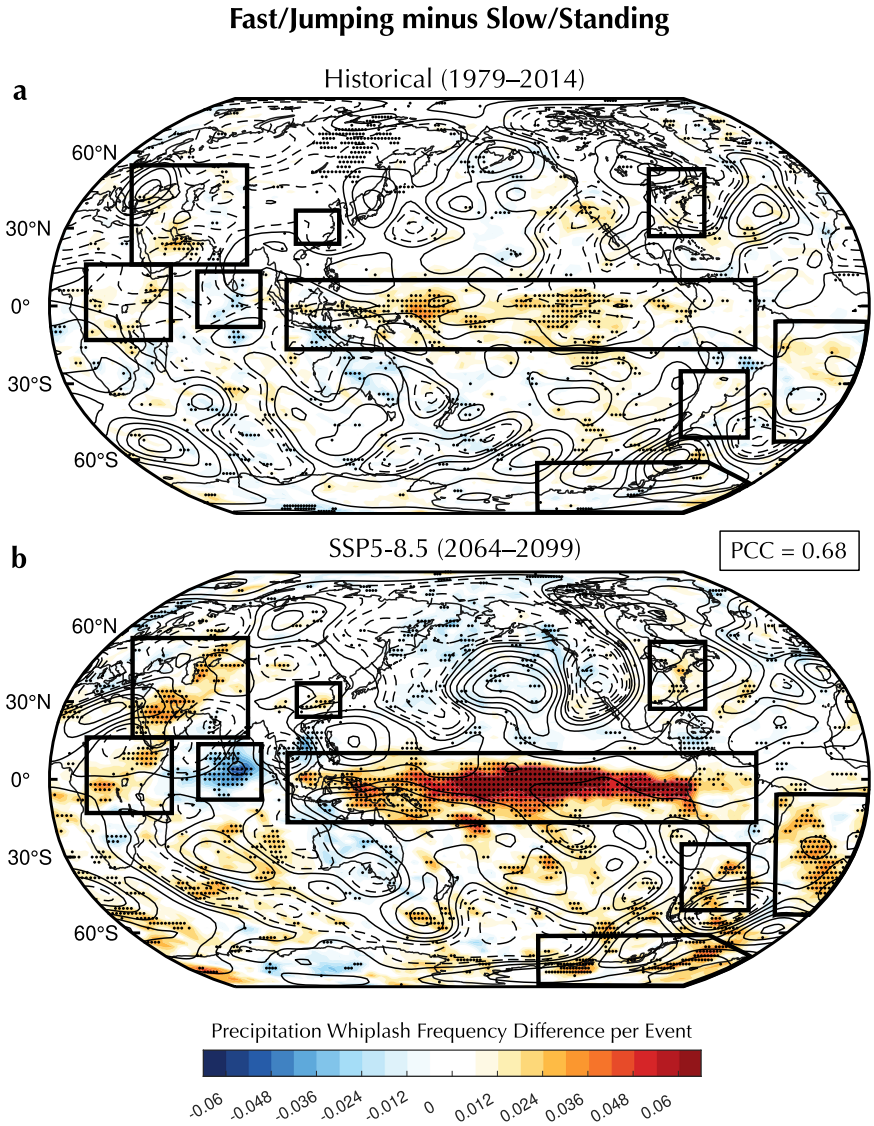

Fig. 3 | Future shift in the difference in precipitation whiplash frequency and circulation variability between fast/jumping and slow/standing Madden-Julian Oscillations (MJOs). a Global map showing the difference in precipitation whiplash frequency (shading; see Methods for definitions) and the 500-hPa streamfunction variability (i.e., standard deviation) (contour, units: 10^5 m^2 s^{-1}) per fast/jumping event compared to that per slow/standing event in the historical simulation (1979–2014) based on the MME12. Stippling denotes that the difference in precipitation whiplash frequency is statistically significant at the 0.05 level across the models (Student's *t* test). Solid (dashed) contours indicate positive (negative) values, with levels from −12 to −2 in an interval of 2, −0.5, 0.5, and from 2 to 12 in an interval of 2 (units: 10^5 m^2 s^{-1}). **b** Similar to panel a, but for the SSP5-8.5 simulation (2064–2099). Global hotspots of the heightened risk of precipitation whiplash are outlined in black. The pattern correlation coefficient of the significant difference in precipitation whiplashes between the historical and future periods is shown in the middle right.

Under the SSP5-8.5 scenario, the R-K ratio of the MJO is projected to plunge by 0.27, from an average of 1.41 to 1.14 (Fig. 4b, c). This change implies that the MJO's Kelvin-Rossby wave couplet shows a disproportionately stronger Kelvin wave easterly to the east of the convection, while the Rossby wave westerly to the west will weaken. Such an alternation suggests an enhanced zonal asymmetry in the wave couplet, which is associated with a future accelerated MJO. To illustrate their relationship further, we construct a scatter plot of the MJO phase speed against the R-K ratio simulated by all 28 CMIP6 models. We show an inverse relationship wherein the smaller the R-K ratio (i.e., the stronger the Kelvin wave response), the faster the eastward propagation speed of the MJO will be (Fig. 5a). The Sen's slope and Mann-Kendall test aptly captures such a relationship, albeit with the existence of outliners. Notably, these outliners, including CanESM5, CMCC-ESM2, MPI-ESM1-2-LR, INM-CM4-8, and INM-CM5-0, are among those that inadequately reproduce MJO propagation and its diverse behavior (Supplementary Fig. 1b).

On the other hand, the background moist GW speed is positively correlated with the MJO phase speed, as adequately represented by most CMIP6 models (Fig. 5b). It is important to note that the changes in the moist GW speed and the horizontal structure (R-K ratio) affect MJO propagation speed independently and jointly. The moist GW speed is an intrinsic geophysical parameter determining the propagation speed of large-scale equatorial waves and MJOs. The Kelvin wave propagates with the GW speed, while the long Rossby wave speed is about one-third of the GW speed[79]. The moist GW speed is collectively determined by the competing effects of dry static stability and moisture destabilization[40]. A more stratified fluid, namely, a more stabilized atmosphere, in this case, would induce a faster internal GW speed[44]. On the other hand, a stronger vertical moisture gradient would instead

https://doi.org/10.1038/s41467-025-58955-4

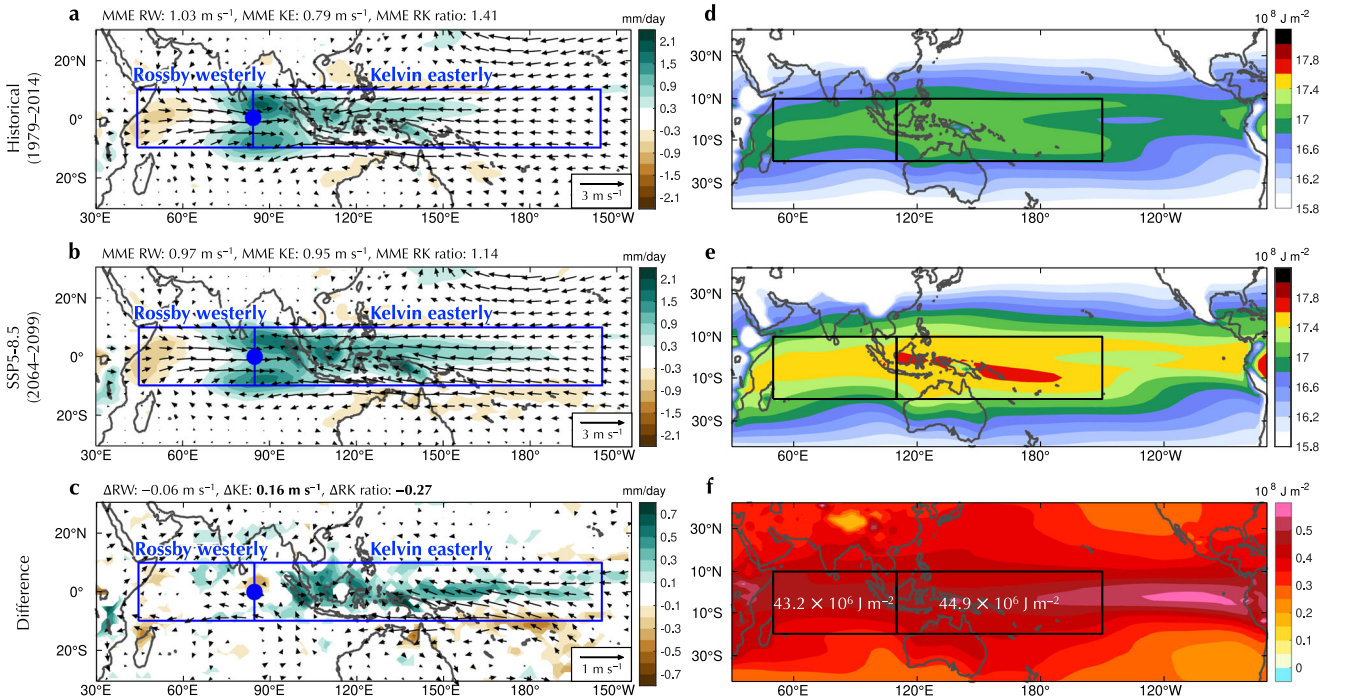

Fig. 4 | Future changes in the Madden-Julian Oscillation (MJO) circulation structure and background mean states. Composites of the mass-weighted integral of the 1000–850-hPa 20–70-day moisture convergence (shading, units: mm day^{-1}) and the 850-hPa winds (vectors, units: m s^{-1}) associated with the MJO events in (**a**) historical (1979–2014) and **b** SSP5-8.5 (2064–2099) scenarios based on the MME12. **c** The difference between the two scenarios, with shading and vectors showing the values with the sign agreed by ≥ 66% of the models. The box region west of the MJO centroid (denoted by a blue dot) refers to the region where the Rossby westerlies (RW) are averaged, while the east of it indicates the region where the Kelvin easterlies (KE) are averaged. **d**–**f** Similar to panels **a**–**c**, but for the background 3-month running mean 1000–500-hPa MSE (units: 10^8 J m^{-2}). The tropical Indian Ocean (20°S–10°N, 50°–110°E) and western-central Pacific Ocean (20°S–10°N, 110°E–150°W) where the MJO convective activity prevailing are outlined in black, with the value showing the regional mean.

slow it down since the latent heat released as moisture condenses can effectively reduce the static stability felt by the wave[45]. Quantitatively, the future change in the moist GW speed, ΔC_1, can be decomposed into the changes in the dry static stability, ΔS_2, and moisture destabilization, $\Delta\bar{q}$, based on our heuristic diagnostic equation (See Methods for definitions and the derivation):

$$\Delta C_1 = \frac{\delta p^2}{4C_1}\left[\left(1 - I + A\bar{q}S_2^{-1}\right)\Delta S_2 - A\Delta\bar{q}\right], \quad (1)$$

The decomposition suggests that the impact of enhanced dry static stability overtakes that of moisture destabilization, yielding a net increase in the moist GW wave speed that aids in the MJO's eastward propagation speed in future warming scenarios (Fig. 5c). The high-emission run sees the strongest effect of enhanced dry static stability offsetting the moisture effect by contributing to 8.39 m s^{-1} (+20.3%) in moist GW wave speed, while moisture destabilization acts to reduce it by 6.26 m s^{-1} (−15.1%) compared to the historical value of the moist GW speed (41.35 m s^{-1}) (Supplementary Fig. 8). The above decomposition is robust, evidenced by a narrow inter-model spread and a negligible residue. A similar result is obtained for the projected changes in the moist GW wave budget under the mitigated scenario (Supplementary Fig. 9). Notably, the increase in the background moist GW speed is not uniform (Supplementary Fig. 8). The GW speed will stay almost the same as its historical value in the tropical eastern Pacific Ocean where moisture destabilization becomes strong enough to completely offset the effect of dry static stability due to the El Niño-like warming (Fig. 4f). In contrast, the slower rate of sea surface warming (SST) warming in the Indian Ocean-western Pacific sector produces a weaker enhancement in the moisture destabilization and is thus dominated by the uniform boost in dry static stability by the GHG forcing (Supplementary Fig. 6). This explains the increased background moist GW speed concerning the EIO MJO acceleration.

However, the acceleration of moist GW speed and the increased skewness of the MJO's Kelvin-Rossby wave couplet cannot account for the MJO acceleration to the fullest. Additional factors must be considered. We notice that the models project more pronounced condensational heating from enhanced precipitation and convection east of future MJO (Supplementary Fig. 10). This asymmetric heating likely results from a more intense BLMC contributed by the accelerated Kelvin wave easterlies (Fig. 4c) and elevated background lower-level specific humidity (Supplementary Fig. 6d). The BLMC favors the development of shallow and congestus clouds east of the MJO's deep convection, forming asymmetric condensational heating that further amplifies the Kelvin-Rossby wave asymmetry for more fast-propagating MJO cases. Further, the increased MJO-coupled dry anomaly in the central and eastern Pacific Ocean suggests an anomalous MJO-related Walker circulation (Supplementary Fig. 10c), promoting equatorial easterly winds and contributing to the development of the BLMC.

The asymmetric diabatic heating coupled with the MJO likely springs from oceanic forcings—an asymmetric equatorial sea surface temperature (SST) warming. Future high-end scenario projects a rise in tropical mean SST by approximately 2.6 °C in an El Niño-like pattern, with the most intense SST warming expected in the equatorial eastern Pacific (Supplementary Fig. 11a–c). One remarkable phenomenon regarding a fast MJO event is its inclination to occur during El Niño episodes[50,81]. Therefore, the mean-state El Niño-like warming in future climates is expected to promote fast-propagating MJO. Existing idealized experiments have demonstrated that a faster propagation of the MJO occurs with an increased zonal scale in response to an eastward extended warm pool[56]. The mean state MSE is an energy source for

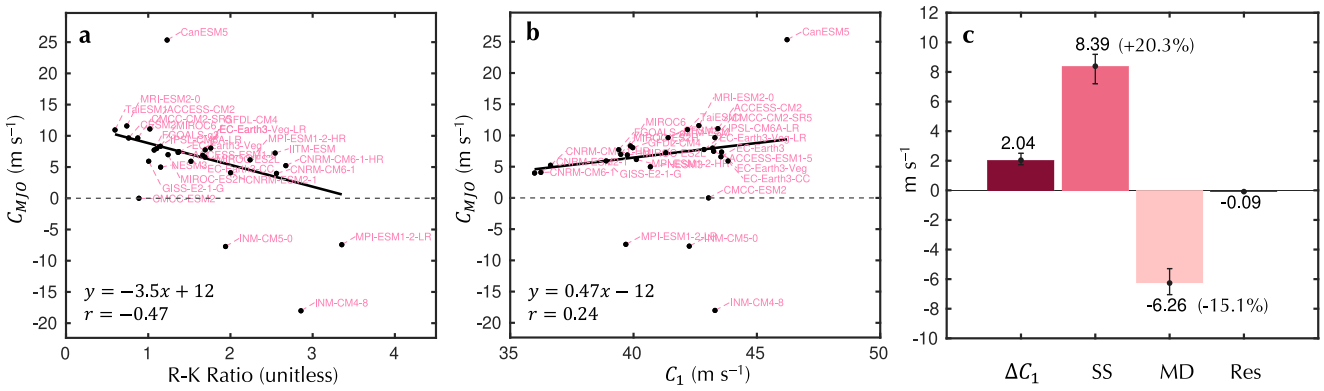

Fig. 5 | Future Madden-Julian Oscillation (MJO) acceleration driven by the stronger effect of warming-induced atmospheric stabilization than moisture destabilization. Scatter plots showing the relationship of the mean MJO propagation speed (C_{MJO}, units: m s^{-1}) against (**a**) the coupled Rossby-Kelvin (R-K) ratio (unitless) and **b** the regional mean-state moist gravity wave (GW) speed (C_1, units: m s^{-1}) averaged over 10°S–10°N, 50°–150°E based on 28 CMIP6 models. The regression is estimated using Sen's slope. The equation and the Kendall rank correlation coefficient are shown on the bottom left. **c** A bar plot showing the effects of static stability (SS) and moisture destabilization (MD) on the future change of moist GW speed (ΔC_1) (units: m s^{-1}) averaged in 10°S–10°N, 50°–150°E during the SSP5-8.5 (2064–2099) scenario, compared to the historical run (1979–2014). The quantities are computed based on the background 3-month running mean fields (see Methods), with the central month being the month of day 0 of each MJO event. The MME12 mean value and the percentage change with respect to the historical regional mean C_1 (41.35 m s^{-1}) are shown, with the uncertainties representing the inter-model spread from the 25th to 75th percentile of the values output by the 12 good models.

MJO development that controls the extent of the convectively coupled equatorial waves[82,83]. We show that the mid-lower tropospheric (1000–500-hPa) MSE is projected to intensify and expand eastward, as most evident in the high-end scenario (Fig. 4d, e). In tandem with the El Niño-like warming, future MSE increase over the maritime continent and the western-central Pacific tends to be higher than in the Indian Ocean (Fig. 4f). We substantiate that this difference is robust by eliminating mean-state differences across the models (Supplementary Fig. 12). The enhanced zonal asymmetry of tropical MSE across the Indo-Pacific basin is expected to stretch the convectively active zone eastward (Supplementary Fig. 5f), enhancing the Kelvin wave response to the east, and deepening the asymmetry of the Kelvin-Rossby couplet (Fig. 4c). These processes, driven by GHG and asymmetric oceanic forcings, collectively clarify the physical origin of the MJO's eastward acceleration in a future warmer climate, as depicted in the schematic diagrams in Fig. 6.

Discussion

Analyzing climate projections from the 12 top-performing CMIP6 models unravels a notable shift in the MJO propagation diversity under anthropogenic GHG warming. A future increase in MJO events is driven primarily by a significant uptick of 40% in fast-propagating events, followed by a 23% rise in jumping events under the far-future SSP5-8.5 scenario, while stationary and slow-moving events are expected to decrease or remain stable. The shifted diversity suggests a less insurmountable barrier to future MJO events in the Maritime Continent as the climate warms. Overall, future MJO events are projected to propagate 22% faster and generate 38% more precipitation over their lifespan than historical events. The predicted growth in fast and jumping events is expected to trigger a global increase in precipitation whiplashes. As the GHG forcing causes a more statically stable atmosphere with a greater water-vapor-holding capacity, our analysis using a simple two-layer model suggests the dominance of increased dry static stability over moisture destabilization in future warmer climates, resulting in faster moist GW and bolstering the MJO eastward acceleration. Hence, contrary to conventional wisdom, we propose that enhanced dry static stability accelerates rather than decelerates the MJO propagation. Additionally, the pivotal oceanic forcing of the mean-state El Niño-like warming will expand the core region of tropical convective instability to the east, thereby increasing the skewness of the MJO's Kelvin-Rossby wave structure and resulting in its future eastward acceleration. Some of these projected trends are already evident in the present-day climate, such as the rapidly expanding Indo-Pacific warm pool[84,85] and the rising frequency of central Pacific El Niño episodes[50,84,86]. These observations provide compelling evidence of the anticipated changes in the MJO diversity based on CMIP6 projections.[87]

What practical insights can we gain from the understanding of the MJO diversity and its impending shift? Firstly, it sheds light on the surging risks of intraseasonal compound hazards. The propagation of MJO heralds alternating pluvial and dry spells[10,88]. The projected increase in fast and jumping events, alongside their eastward acceleration and heavier precipitation intensity, are expected to reduce the interval between wet and drought conditions, leading to greater weather fluctuations and the emergence of MJO-coupled precipitation whiplash hotspots globally (Fig. 3). These challenges can severely impact the climate resilience of existing infrastructure and should be carefully considered in future agricultural practices, urban planning, multi-hazard early warning systems, and climate mitigation. On exposure and vulnerability, the global population is expected to rise from 8 billion to between 9.4 and 12.7 billion by 2100, with an unprecedented increase in the proportion of elderly individuals reaching 22.4%[89,90]. The combination of demographic growth and aging foreshadows a greater impact of the emerging subseasonal precipitation whiplashes associated with the far-reaching impacts of the changing MJO diversity.

The good news is that fast-propagating MJO tends to be more predictable than other propagation archetypes. Drawn from a 20-year, ten-ensemble S2S hindcast by the Geophysical Fluid Dynamics Laboratory (GFDL) Seamless System for Prediction and Earth System Research (SPEAR) coupled model, a recent report[28] uncovered that fast-propagating MJO events had the highest prediction skill, achieving accuracy up to 38 days in advance. In contrast, slow-moving and jumping events demonstrated a prediction skill of 31 days, while the standing events were the least predictable, with a lead time of only 23 days. Similar results were attained based on another global climate model[91]. Hence, forecasting the ever-growing, fast-moving MJO events in a warmer climate will promisingly push the current prediction limit closer to the maximum attainable range of 35–45 days shown by modern S2S forecasting systems[92]. However, future improvement in MJO forecasting hinges ultimately on the capability of S2S prediction models to accurately simulate the MJO diversity and its evolving patterns. Models that can capture the fast and jumping events and their

https://doi.org/10.1038/s41467-025-58955-4

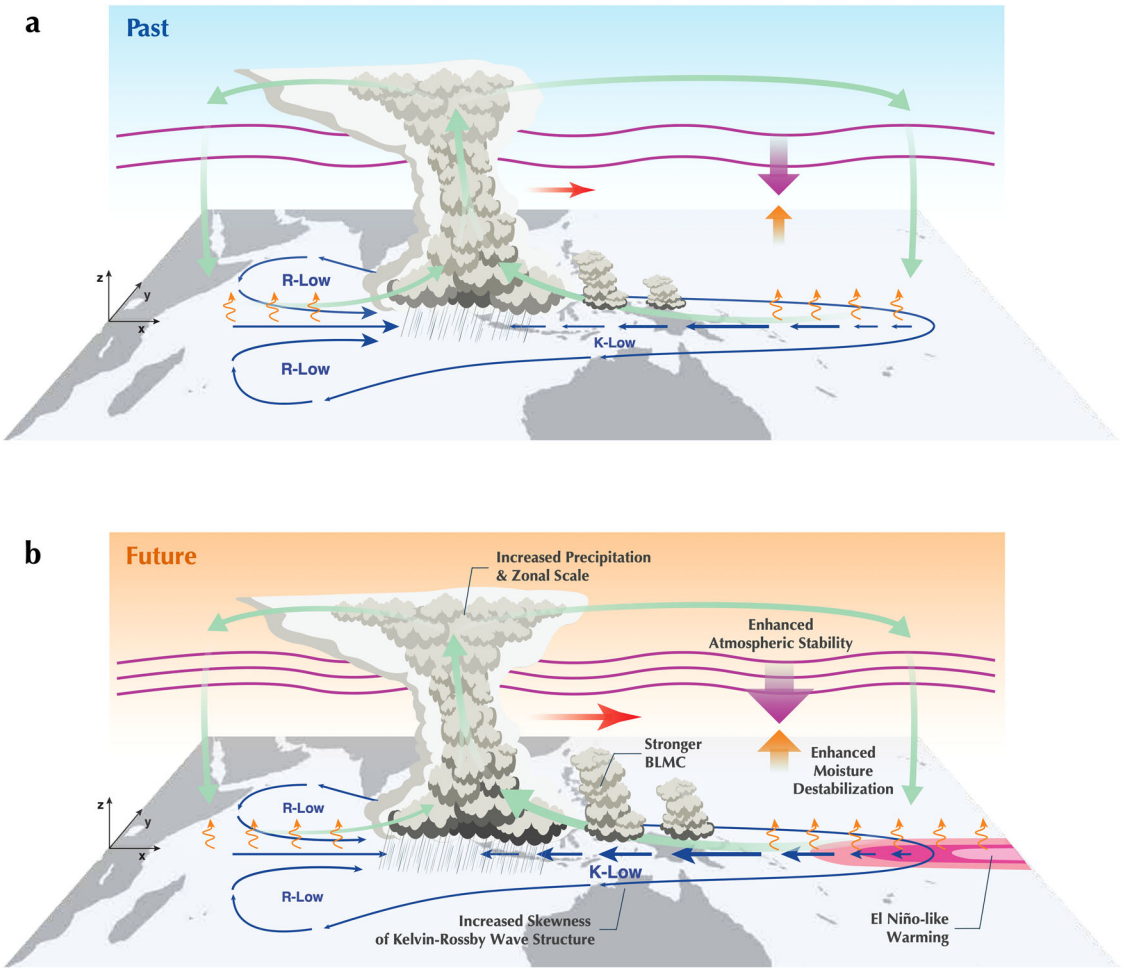

Fig. 6 | Key physical processes associated with the Madden-Julian Oscillation (MJO)'s eastward acceleration. Schematic diagrams depicting the three-dimensional structure of the MJO and its dynamics (**a**), in the past and (**b**), in future warmer climates. Panel b details the key changes in the physical processes that contribute to the MJO's eastward acceleration. BLMC stands for boundary-layer moisture convergence.

trends will likely extend their prediction range beyond four to five weeks, providing more time for decision-making in hazard preparedness and emergency response to minimize casualties and property damage.

The conceptual framework of MJO diversity has been instrumental in identifying physical processes responsible for propagation-type changes and in uncovering model deficiencies. The good and poor CMIP6 models, chosen based on their reproducibility of the historical MJO diversity (Supplementary Fig. 1b), align well with those selected by lag-regression diagnostic[49], wave spectrum[93], or sophisticated criteria of moisture-mode properties[94]. The agreement upon model selection reveals two important insights: On the one hand, accurately simulating the moist processes and coupled equatorial wave structure could be the key to reproduce the various facets of the MJO propagation diversity. On the other hand, evaluating model performance in reproducing the historical MJO diversity can be a simple and straightforward technique for distinguishing good models from poor ones. CMIP6 models tend to simulate more standing and jumping but fewer propagating cases than observations (Supplementary Fig. 4). Even for the good models at higher spatial resolutions, the simulated intraseasonal OLR variability of the propagating events is apparently weaker than observations. These common biases in MJO propagation diversity and variability suggest critical gaps in fundamental model physics, such as improper parameterizations of the coupling between shallow convection and boundary-layer circulation[55,72,78] and Kelvin wave response[55,56,61,93], as well as a relatively limited understanding of the Maritime Continent's impact on the MJO propagation[49,95]. Addressing these grand challenges in numerical simulations can be of utmost importance for advancing the prediction of the growing prevalence of hazard-triggering fast and jumping MJO events in a warmer world.

In this study, the explanation of the physical processes changing MJO propagation was underpinned by the trio-interaction theory. However, several other theories have also been proposed in the literature[40,41,54,57,60,96–99]. Among them, four theories specifically address the MJO's propagation and selection mechanisms for the spatial and temporal scales[87]: the skeleton theory[54], the 'moisture-mode' theory[60], the gravity-wave theory[100], and the trio-interaction theory[57]. One fundamental feature discovered by Madden and Julian (1972)[2]—which was not used to verify the theories—is the sea-level low pressure is ahead of eastward propagating MJO convection. Numerous observational studies have shown that the boundary layer convergence associated with the low-pressure anomaly leads the MJO, which shows a salient vertical tilted structure against its propagation in the fields of MSE, specific humidity, and vertical velocity[42,64,72,78,101,102]. This vertical structure and the characteristic coupled Rossby-Kelvin wave structure are essential for verifying the theories. Among the four theories, only the trio-interaction theory effectively captures the characteristic vertical and horizontal structure by incorporating the boundary layer dynamics and convective interaction with the Kelvin and Rossby waves. The trio-interaction theory unravels an inherent linkage between the MJO circulation structure and its eastward propagation. It suggests that

different cumulus parameterization schemes can lead to different R-K ratios and, thus, different propagation speeds. The skeleton theory and moisture-mode theory can be viewed as a special form of the trio-interaction under a generalized theoretical framework that uses different cumulus parameterization schemes[42]. Various theories may interpret MJO eastward propagation speed differently. For instance, in the "moisture-mode" theory, the eastward propagation of the MJO is mainly maintained by large-scale horizontal and vertical moisture advection[58–60]. This theory would interpret the future rise in fast-moving MJO events as the result of an increased horizontal advection of moisture that causes a positive column- or lower troposphere-integrated moisture (or MSE) tendency to the east[34,47,83,103]. However, the positive moisture tendency ahead of MJO can arise from both the intensification of the MJO convection and its eastward movement, making it a less clear indicator of propagation speed. It may also overlook the impact of dry static stability in accelerating moist GW waves and the MJO. Future research on aspects such as the extent to which the BL frictional coupled Kelvin-Rossby feedback is important compared to other processes, such as moisture and cloud-radiative feedback, in both the present and future climates, will facilitate the reconciliation of existing theories and further advance our understanding of future changes in MJO diversity and dynamics.

Methods

Observational datasets and reanalysis

The satellite-based National Oceanic and Atmospheric Administration (NOAA)-interpolated OLR dataset[104] is adopted as a benchmark to evaluate CMIP6 model performance in simulating the MJO diversity. The hourly, 1° × 1° pressure-level and surface environmental fields are retrieved from the fifth-generation European Centre for Medium-Range Weather Forecast (ECMWF) reanalysis (ERA5)[105] for diagnosis. Leap days are omitted from all observational and reanalysis datasets, as most CMIP6 models use a 365-day calendar. Given its superior advantages over the other filters[106], a 20–70-day band-pass Butterworth filter is adopted to extract the intraseasonal anomalies from the daily data for MJO event detection and analysis. A 3-point zonal running mean is applied to all analyses to remove small-scale noises[50]. The mean state is computed based on the period of interest. The extraction of intraseasonal anomalies is independent of the mean state.

CMIP6 models and experiments

The CMIP6 archive provides state-of-the-art climate projections in response to anthropogenic and natural forcings. Here we examined 28 CMIP6 models (Supplementary Table 1) with complete output of daily outgoing longwave radiation available—the key proxy for identifying the MJO-related disturbances[10]. Models based on a 360-day calendar were omitted from our analyses. Experiments considered here are historical (with all natural and anthropogenic forcings), a mitigated scenario that produces a radiative forcing at 4.5 W m^{-2} in 2100 (SSP2-4.5), and a high-emission scenario that produces a radiative forcing at 8.5 W m^{-2} in 2100 (SSP5-8.5)[70].

Detection of MJO events and propagation diversity

Following Wang et al. (2019)[50], an MJO event was identified if the regional mean 20–70-day OLR anomaly over the eastern Indian Ocean (EIO; 10°S–10°N, 75°–95°E) was negative and had a magnitude greater than one S.D. for five consecutive days during the boreal cold season (from November through April). The event day 0 was chosen when the averaged OLR anomaly reached the minimum. We then computed the 10°S–10°N averaged lag-longitude diagrams (from day −10 to day 20 and 60°E to 180°) of each event, which were smoothed by a 3-point zonal running mean and with the OLR anomalies greater than −5 W m^{-2} set to zeros. k-means clustering[107] with the correlation distance metric was then applied to the smoothed lag-longitude diagrams to assign events to four clusters. The clustering was iterated for a maximum of 10,000 times to achieve convergence, and the run was repeated 10 million times with random initializations to select the optimal clustering with the minimum total sum of distances. Among the 105 MJO events over the EIO using NOAA-interpolated OLR from 1979 to 2014, we retained 88 that are considerably well-matched to the centroid of their clusters with a Silhouette score greater or equal to 0.06. The composites of the well-match events reconstruct the four MJO propagation archetypes (Supplementary Fig. 4b–e), which serve as benchmarks for matching the MJO propagation patterns from CMIP6 simulations.

Matching CMIP6 MJO events to the four archetypes

The k-means method is an iterative algorithm that seeks to minimize the average square distance between points within the same cluster[108]. The classification results are therefore entirely subject to the inherent structure and bias of the data fed into the algorithm. For this reason, the four k-means clusters derived from a CMIP6 model simulation would differ from the four MJO archetypes from observational data. To permit a simple, objective, and effective assignment of the CMIP6 MJO events to the four archetypes, we matched them to the most similar archetype based on the highest pattern correlation coefficient (PCC) between its lag-longitude pattern and the four benchmark patterns. After the matching, we evaluate the model performance in simulating the historical MJO diversity by concatenating the composites of the four propagation patterns based on the CMIP6 historical simulations and compared them against the four benchmarks simultaneously (Supplementary Fig. 1a). The 12 top-performing models exhibiting a normalized RMSE less than 0.3 were selected for the main analysis of this study (Supplementary Fig. 1b). The six poor models with a normalized RMSE of greater than 0.6 were selected for comparison and discussion.

Regression-based approach in estimating MJO propagation speed

The MJO propagation speed was measured based on the lag-longitude OLR diagram using the following procedures. Firstly, we identify the largest deep convection with the OLR anomaly less than −3 W m^{-2} in the diagram. Secondly, we locate the points with minimum OLR anomaly at each longitude of the object. Thirdly, we perform simple linear regression on these points to obtain Sen's slope, which is resistant to outliers and more robust than an ordinary least-square fit[109]. The statistical significance of the slope is verified by the non-parametric Mann-Kendall test[110–112]. With appropriate unit conversion, the inverse of the slope coefficient yields the phase speed of the MJO event.

MJO-related precipitation whiplash

Precipitation whiplash refers to a sudden transition between wet and dry extremes[22–26]. Previous studies defined precipitation whiplash on a year-to-year basis, but none have examined its connection to the MJO on the S2S timescale. Here, we identify a wet-to-dry event when 20–70-day precipitation exceeds the 99th percentile of the historical values (1979–2014), followed by a dry event below the 1st percentile value, and vice versa for a dry-to-wet event. These wet-to-dry and dry-to-wet events collectively constitute precipitation whiplashes. A subseasonal precipitation whiplash event is considered MJO-related if it takes place from day −15 to day 15 of an MJO event.

Moist GW speed diagnosis

The source of contributions to the convectively coupled, moist GW wave speed can be diagnosed and quantified using a simple two-layer model[40]. Assuming a trivial effect of evaporation on the GW, ignoring Newtonian cooling and the boundary-layer terms and restoring the dimensions, the combined thermodynamic and moisture equation can

be simplified as

$$\frac{\partial \phi}{\partial t} + C_0^2(1-I)\left(\frac{\partial u}{\partial x} + \frac{\partial v}{\partial y}\right) = 0, \tag{2}$$

where ϕ, u, v denote the baroclinic component of geopotential, zonal wind, and meridional wind; C_0 denotes the dry GW speed, and the dimensionless parameter I refers to the coefficient of heating contributed by the wave convergence. The moist GW speed C_1 is then measured by

$$C_1^2 = C_0^2(1-I), \tag{3}$$

where the dimensionless parameter I is given by

$$I = \frac{\bar{q}}{\alpha}, \tag{4}$$

where $\bar{q}$ is the difference between the vertical mean of specific humidity in the lower atmosphere (500–1000 hPa; $\bar{q}_3$) and the upper atmosphere (0–500 hPa; $\bar{q}_1$), namely,

$$\bar{q} \equiv \bar{q}_3 - \bar{q}_1. \tag{5}$$

In a completely dry atmosphere, the GW speed would reduce to C_0. The non-dimensional measure of dry static stability α writes

$$\alpha = \frac{2C_p p_2 C_0^2}{RbL_c \delta p}, \tag{6}$$

where R is the specific gas constant for dry air (287 J kg^{-1} K^{-1}), L_c is the latent heat of condensation (2.26×10^6 J kg^{-1}), b is the fractional conversion coefficient of moisture into rainfall (taken as 0.9), δp is the half-depth of the atmosphere (500 hPa), C_p is the specific heat at constant pressure (1004 J kg^{-1} K^{-1}), and p_2 is the pressure in the middle of the free atmosphere (500 hPa). Our sensitivity test showed that the choice of b does not affect the result of a stronger effect of dry static stability than moisture destabilization in future GW speed. The dry GW speed of the gravest baroclinic mode can be measured by

$$C_0 = \left(\frac{S_2 \delta p^2}{2}\right)^{1/2}, \tag{7}$$

where S_2 refers to the 500-hPa static stability parameter (units: m^2 s^{-2} Pa^{-2}) estimated by $\frac{1}{\theta_2 \rho_2}\frac{\theta_1-\theta_3}{p_1-p_3}$, with ρ_2 being the basic-state air density at 500 hPa. Since CMIP6 output does not contain data at 750 hPa, potential temperatures θ_1, θ_2 and θ_3 are taken as those at 250, 500, and 700 hPa, respectively.

Differentiating both sides of Eq. (3) between two periods of time, the future change of the dimensionless parameter I can be expressed as

$$\Delta C_1 = \frac{1}{2(C_1)_h}\left[\Delta C_0^2(1-I_h) - \left(C_0^2\right)_h \Delta I\right], \tag{8}$$

Where $\Delta \equiv (\cdot)_f - (\cdot)_h$, with the subscript f and h denote the mean quantity in the future and historical periods, respectively.

Dropping the subscript h for simplicity and differentiating Eq. (7) gives

$$\Delta C_0^2 = \frac{\delta p^2}{2}\Delta S_2. \tag{9}$$

Similarly, the future change of I writes

$$\Delta I = A\left(S_2^{-1}\Delta \bar{q} - \bar{q}S_2^{-2}\Delta S_2\right), \tag{10}$$

where $A = \frac{RbL_c}{C_p p_2 \delta p}$. Substituting Eqs. (9) and (10) into Eq. (8) gives the budgets from the future change in the moist GW speed:

$$\Delta C_1 = \frac{\delta p^2}{4C_1}\left[\left(1 - I + A\bar{q}S_2^{-1}\right)\Delta S_2 - A\Delta \bar{q}\right], \tag{11}$$

The first and second terms on the right-hand side of Eq. (11) represent the effects of static stability and moisture destabilization, respectively. Equation (11) provides useful physical insights into the competition between the dry static stability and the moisture effect on the moist GW speed.

Data availability

Source data supporting the results are available from the Zenodo repository at https://doi.org/10.5281/zenodo.15099888. The NOAA-interpolated OLR dataset[104] provided by the NOAA PSL, Boulder, Colorado, USA, is available from their website at https://psl.noaa.gov/data/gridded/data.olrcdr.interp.html. ERA5 reanalysis[105] is available at https://doi.org/10.24381/cds.adbb2d47. CMIP6 model simulation output[113] is available at https://esgf-node.llnl.gov/projects/cmip6/.

Code availability

The source code for reproducing the analyses here is available from the Zenodo repository at https://doi.org/10.5281/zenodo.15099888. Geographic figures were generated using a Matlab package M_Map[114], available at www.eoas.ubc.ca/~rich/map.html.

References

1. Madden, R. A. & Julian, P. R. Detection of a 40–50 Day Oscillation in the Zonal Wind in the Tropical Pacific. *J. Atmos. Sci.* **28**, 702–708 (1971).
2. Madden, R. A. & Julian, P. R. Description of Global-Scale Circulation Cells in the Tropics with a 40–50 Day Period. *J. Atmos. Sci.* **29**, 1109–1123 (1972).
3. Slingo, J. M., Rowell, D. P., Sperber, K. R. & Nortley, F. On the predictability of the interannual behaviour of the Madden-Julian oscillation and its relationship with el Niño. *Q. J. R. Meteorological Soc.* **125**, 583–609 (1999).
4. Kessler, W. S. EOF Representations of the Madden–Julian Oscillation and Its Connection with ENSO*. *J. Clim.* **14**, 3055–3061 (2001).
5. Stan, C. et al. Review of Tropical-Extratropical Teleconnections on Intraseasonal Time Scales. *Rev. Geophys.* **55**, 902–937 (2017).
6. Donald, A. et al. Near-global impact of the Madden-Julian Oscillation on rainfall. *Geophys. Res. Lett.* **33**, L09704 (2006).
7. Zhang, C. Madden–Julian Oscillation: Bridging Weather and Climate. *Bull. Am. Meteorol. Soc.* **94**, 1849–1870 (2013).
8. Jones, C., Waliser, D. E., Lau, K. M. & Stern, W. Global Occurrences of Extreme Precipitation and the Madden–Julian Oscillation: Observations and Predictability. *J. Clim.* **17**, 4575–4589 (2004).
9. Wang, B. & Moon, J.-Y. An Anomalous Genesis Potential Index for MJO Modulation of Tropical Cyclones. *J. Clim.* **30**, 4021–4035 (2017).
10. Wheeler, M. C. & Hendon, H. H. An all-season real-time multivariate MJO index: Development of an index for monitoring and prediction. *Mon. Weather Rev.* **132**, 1917–1932 (2004).
11. Liu, F. et al. Intraseasonal variability of global land monsoon precipitation and its recent trend. *NPJ Clim. Atmos. Sci.* **5**, 30 (2022).
12. Moon, J.-Y., Wang, B. & Ha, K.-J. ENSO regulation of MJO teleconnection. *Clim. Dyn.* **37**, 1133–1149 (2011).

13. Riddle, E. E. et al. The impact of the MJO on clusters of wintertime circulation anomalies over the North American region. *Clim. Dyn.* **40**, 1749–1766 (2013).
14. Chen, G. Diversity of the Global Teleconnections Associated with the Madden–Julian Oscillation. *J. Clim.* **34**, 397–414 (2021).
15. Guan, B., Waliser, D. E., Molotch, N. P., Fetzer, E. J. & Neiman, P. J. Does the Madden–Julian Oscillation Influence Wintertime Atmospheric Rivers and Snowpack in the Sierra Nevada? *Mon. Weather Rev.* **140**, 325–342 (2012).
16. Mundhenk, B. D., Barnes, E. A. & Maloney, E. D. All-Season Climatology and Variability of Atmospheric River Frequencies over the North Pacific. *J. Clim.* **29**, 4885–4903 (2016).
17. Yoo, C., Feldstein, S. & Lee, S. The impact of the Madden-Julian Oscillation trend on the Arctic amplification of surface air temperature during the 1979-2008 boreal winter. *Geophys. Res. Lett.* **38**, n/a–n/a (2011).
18. Moore, A. M. & Kleeman, R. Stochastic Forcing of ENSO by the Intraseasonal Oscillation. *J. Clim.* **12**, 1199–1220 (1999).
19. Puy, M., Vialard, J., Lengaigne, M. & Guilyardi, E. Modulation of equatorial Pacific westerly/easterly wind events by the Madden–Julian oscillation and convectively-coupled Rossby waves. *Clim. Dyn.* **46**, 2155–2178 (2016).
20. Chang, C.-W. J., Hsu, H.-H., Cheah, W., Tseng, W.-L. & Jiang, L.-C. Madden–Julian Oscillation Enhances Phytoplankton Biomass in the Maritime Continent. *Sci. Rep.* **9**, 5421 (2019).
21. Waliser, D. E., Murtugudde, R., Strutton, P. & Li, J. Subseasonal organization of ocean chlorophyll: Prospects for prediction based on the Madden-Julian Oscillation. *Geophys. Res. Lett.* **32**, L23602 (2005).
22. Swain, D. L., Langenbrunner, B., Neelin, J. D. & Hall, A. Increasing precipitation volatility in twenty-first-century California. *Nat. Clim. Chang* **8**, 427–433 (2018).
23. Chen, D., Norris, J., Thackeray, C. & Hall, A. Increasing precipitation whiplash in climate change hotspots. *Environ. Res. Lett.* **17**, 124011 (2022).
24. Dai, L., Cheng, T. F. & Lu, M. Anthropogenic warming disrupts intraseasonal monsoon stages and brings dry-get-wetter climate in future East Asia. *NPJ Clim. Atmos. Sci.* **5**, 11 (2022).
25. Fang, B. & Lu, M. Asia Faces a Growing Threat From Intraseasonal Compound Weather Whiplash. *Earths Fut.* **11**, e2022EF003111 (2023).
26. Tan, X. et al. Increasing global precipitation whiplash due to anthropogenic greenhouse gas emissions. *Nat. Commun.* **14**, 2796 (2023).
27. Vitart, F. & Robertson, A. W. The sub-seasonal to seasonal prediction project (S2S) and the prediction of extreme events. *NPJ Clim. Atmos. Sci.* **1**, 1–7 (2018).
28. Xiang, B. et al. S2S Prediction in GFDL SPEAR: MJO Diversity and Teleconnections. *Bull. Am. Meteorol. Soc.* **103**, E463–E484 (2022).
29. Arnold, N. P., Kuang, Z. & Tziperman, E. Enhanced MJO-like Variability at High SST. *J. Clim.* **26**, 988–1001 (2013).
30. Chang, C. J., Tseng, W., Hsu, H., Keenlyside, N. & Tsuang, B. The Madden-Julian Oscillation in a warmer world. *Geophys. Res. Lett.* **42**, 6034–6042 (2015).
31. Adames, Á. F., Kim, D., Sobel, A. H., Del Genio, A. & Wu, J. Changes in the structure and propagation of the MJO with increasing CO2. *J. Adv. Model Earth Syst.* **9**, 1251–1268 (2017).
32. Bui, H. X. & Maloney, E. D. Changes in Madden-Julian Oscillation Precipitation and Wind Variance Under Global Warming. *Geophys. Res. Lett.* **45**, 7148–7155 (2018).
33. Maloney, E. D., Adames, Á. F. & Bui, H. X. Madden–Julian oscillation changes under anthropogenic warming. *Nat. Clim. Chang* **9**, 26–33 (2019).
34. Cui, J. & Li, T. Changes of MJO propagation characteristics under global warming. *Clim. Dyn.* **53**, 5311–5327 (2019).
35. Zhou, W., Yang, D., Xie, S.-P. & Ma, J. Amplified Madden–Julian oscillation impacts in the Pacific–North America region. *Nat. Clim. Chang* **10**, 654–660 (2020).
36. Bui, H. X. et al. Emergence of Madden-Julian oscillation precipitation and wind amplitude changes in a warming climate. *NPJ Clim. Atmos. Sci.* **6**, 22 (2023).
37. Arnold, N. P., Branson, M., Kuang, Z., Randall, D. A. & Tziperman, E. MJO Intensification with Warming in the Superparameterized CESM. *J. Clim.* **28**, 2706–2724 (2015).
38. Wolding, B. O., Maloney, E. D., Henderson, S. & Branson, M. Climate change and the Madden-Julian Oscillation: A vertically resolved weak temperature gradient analysis. *J. Adv. Model Earth Syst.* **9**, 307–331 (2017).
39. Rushley, S. S., Kim, D. & Adames, Á. F. Changes in the MJO under Greenhouse Gas–Induced Warming in CMIP5 Models. *J. Clim.* **32**, 803–821 (2019).
40. Wang, B. Dynamics of Tropical Low-Frequency Waves: An Analysis of the Moist Kelvin Wave. *J. Atmos. Sci.* **45**, 2051–2065 (1988).
41. Lau, K.-M. & Peng, L. Origin of Low-Frequency (Intraseasonal) Oscillations in the Tropical Atmosphere. Part I: Basic Theory. *J. Atmos. Sci.* **44**, 950–972 (1987).
42. Wang, B. & Chen, G. A general theoretical framework for understanding essential dynamics of Madden–Julian oscillation. *Clim. Dyn.* **49**, 2309–2328 (2017).
43. Trenberth, K. E., Dai, A., Rasmussen, R. M. & Parsons, D. B. The Changing Character of Precipitation. *Bull. Am. Meteorol. Soc.* **84**, 1205–1217 (2003).
44. Holton, J. R. *An Introduction to Dynamic Meteorology* (Elsevier Academic Press, 2004).
45. Frierson, D. M. W. Convectively Coupled Kelvin Waves in an Idealized Moist General Circulation Model. *J. Atmos. Sci.* **64**, 2076–2090 (2007).
46. Matthews, A. J. Primary and successive events in the Madden–Julian Oscillation. *Q. J. R. Meteorological Soc.* **134**, 439–453 (2008).
47. Kim, D., Kug, J.-S. & Sobel, A. H. Propagating versus Nonpropagating Madden–Julian Oscillation Events. *J. Clim.* **27**, 111–125 (2014).
48. Zhang, C. & Ling, J. Barrier Effect of the Indo-Pacific Maritime Continent on the MJO: Perspectives from Tracking MJO Precipitation. *J. Clim.* **30**, 3439–3459 (2017).
49. Ahn, M. et al. MJO Propagation Across the Maritime Continent: Are CMIP6 Models Better Than CMIP5 Models? *Geophys. Res. Lett.* **47**, e2020GL087250 (2020).
50. Wang, B., Chen, G. & Liu, F. Diversity of the Madden-Julian Oscillation. *Sci. Adv.* **5**, eaax0220 (2019).
51. Raymond, D. J. A New Model of the Madden–Julian Oscillation. *J. Atmos. Sci.* **58**, 2807–2819 (2001).
52. Fuchs, Z. & Raymond, D. J. Large-Scale Modes in a Rotating Atmosphere with Radiative–Convective Instability and WISHE. *J. Atmos. Sci.* **62**, 4084–4094 (2005).
53. Fuchs, Ž. & Raymond, D. J. A simple model of intraseasonal oscillations. *J. Adv. Model Earth Syst.* **9**, 1195–1211 (2017).
54. Majda, A. J. & Stechmann, S. N. The skeleton of tropical intraseasonal oscillations. *Proc. Natl Acad. Sci.* **106**, 8417–8422 (2009).
55. Chen, G. & Wang, B. Dynamic moisture mode versus moisture mode in MJO dynamics: importance of the wave feedback and boundary layer convergence feedback. *Clim. Dyn.* **52**, 5127–5143 (2019).
56. Chen, G. & Wang, B. Circulation Factors Determining the Propagation Speed of the Madden–Julian Oscillation. *J. Clim.* **33**, 3367–3380 (2020).
57. Wang, B., Liu, F. & Chen, G. A trio-interaction theory for Madden–Julian oscillation. *Geosci. Lett.* **3**, 1–16 (2016).
58. Sobel, A. & Maloney, E. An Idealized Semi-Empirical Framework for Modeling the Madden–Julian Oscillation. *J. Atmos. Sci.* **69**, 1691–1705 (2012).

59. Sobel, A. & Maloney, E. Moisture Modes and the Eastward Propagation of the MJO. *J. Atmos. Sci.* **70**, 187–192 (2013).
60. Adames, Á. F. & Kim, D. The MJO as a Dispersive, Convectively Coupled Moisture Wave: Theory and Observations. *J. Atmos. Sci.* **73**, 913–941 (2016).
61. Wang, B. & Lee, S.-S. MJO Propagation Shaped by Zonal Asymmetric Structures: Results from 24 GCM Simulations. *J. Clim.* **30**, 7933–7952 (2017).
62. Madden, R. A. Seasonal Variations of the 40-50 Day Oscillation in the Tropics. *J. Atmos. Sci.* **43**, 3138–3158 (1986).
63. Maloney, E. D. & Hartmann, D. L. Frictional Moisture Convergence in a Composite Life Cycle of the Madden–Julian Oscillation. *J. Clim.* **11**, 2387–2403 (1998).
64. Sperber, K. R. Propagation and the Vertical Structure of the Madden–Julian Oscillation. *Mon. Weather Rev.* **131**, 3018–3037 (2003).
65. Adames, Á. F. & Wallace, J. M. Three-Dimensional Structure and Evolution of the Vertical Velocity and Divergence Fields in the MJO. *J. Atmos. Sci.* **71**, 4661–4681 (2014).
66. Adames, Á. F. & Wallace, J. M. Three-Dimensional Structure and Evolution of the Moisture Field in the MJO. *J. Atmos. Sci.* **72**, 3733–3754 (2015).
67. Rui, H. & Wang, B. Development Characteristics and Dynamic Structure of Tropical Intraseasonal Convection Anomalies. *J. Atmos. Sci.* **47**, 357–379 (1990).
68. Gonzalez, A. O. & Jiang, X. Distinct Propagation Characteristics of Intraseasonal Variability Over the Tropical West Pacific. *J. Geophys. Res. Atmos.* **124**, 5332–5351 (2019).
69. Wei, Y., Ren, H., Duan, W. & Sun, G. Westward-Propagating Disturbances Shape Diverse MJO Propagation. *Geophys. Res. Lett.* **50**, e2023GL104778 (2023).
70. O'Neill, B. C. et al. The Scenario Model Intercomparison Project (ScenarioMIP) for CMIP6. *Geosci. Model Dev.* **9**, 3461–3482 (2016).
71. Swain, D. L. et al. Hydroclimate volatility on a warming Earth. *Nat. Rev. Earth Environ.* **6**, 35–50 (2025).
72. Wang, B. et al. Dynamics-oriented diagnostics for the Madden-Julian Oscillation. *J. Clim*. https://doi.org/10.1175/JCLI-D-17-0332.1 (2018).
73. Ling, J., Zhao, Y. & Chen, G. Barrier Effect on MJO Propagation by the Maritime Continent in the MJO Task Force/GEWEX Atmospheric System Study Models. *J. Clim.* **32**, 5529–5547 (2019).
74. Kim, D., Sobel, A. H., Maloney, E. D., Frierson, D. M. W. & Kang, I.-S. A Systematic Relationship between Intraseasonal Variability and Mean State Bias in AGCM Simulations. *J. Clim.* **24**, 5506–5520 (2011).
75. Gonzalez, A. O. & Jiang, X. Winter mean lower tropospheric moisture over the Maritime Continent as a climate model diagnostic metric for the propagation of the Madden-Julian oscillation. *Geophys. Res. Lett.* **44**, 2588–2596 (2017).
76. Back, S.-Y., Kim, D. & Son, S.-W. MJO Diversity in CMIP6 Models. *J. Clim.* **37**, 4835–4850 (2024).
77. Hoskins, B. J. & Karoly, D. J. The Steady Linear Response of a Spherical Atmosphere to Thermal and Orographic Forcing. *J. Atmos. Sci.* **38**, 1179–1196 (1981).
78. Jiang, X. et al. Vertical structure and physical processes of the Madden-Julian oscillation: Exploring key model physics in climate simulations. *J. Geophys. Res. Atmos.* **120**, 4718–4748 (2015).
79. Matsuno, T. Quasi-Geostrophic Motions in the Equatorial Area. *J. Meteorological Soc. Jpn. Ser. II* **44**, 25–43 (1966).
80. Gill, A. E. Some simple solutions for heat-induced tropical circulation. *Q. J. R. Meteorological Soc.* **106**, 447–462 (1980).
81. Wei, Y. & Ren, H.-L. Modulation of ENSO on Fast and Slow MJO Modes during Boreal Winter. *J. Clim.* **32**, 7483–7506 (2019).
82. Wang, B. & Xie, X. A Model for the Boreal Summer Intraseasonal Oscillation. *J. Atmos. Sci.* **54**, 72–86 (1997).
83. Maloney, E. D. The moist static energy budget of a composite tropical intraseasonal oscillation in a climate model. *J. Clim.* **22**, 711–729 (2009).
84. Cai, W. et al. Increasing frequency of extreme El Niño events due to greenhouse warming. *Nat. Clim. Chang* **4**, 111–116 (2014).
85. Roxy, M. K. et al. Twofold expansion of the Indo-Pacific warm pool warps the MJO life cycle. *Nature* **575**, 647–651 (2019).
86. Yeh, S.-W. et al. El Niño in a changing climate. *Nature* **461**, 511–514 (2009).
87. Zhang, C., Adames, Á. F., Khouider, B., Wang, B. & Yang, D. Four Theories of the Madden-Julian Oscillation. *Rev. Geophys.* **58**, e2019RG000685 (2020).
88. Wang, B. et al. Climatological Madden-Julian Oscillation during boreal spring leads to abrupt Australian monsoon retreat and Asian monsoon onsets. *NPJ Clim. Atmos. Sci.* **7**, 40 (2024).
89. Cleland, J. World Population Growth; Past, Present and Future. *Environ. Resour. Econ. (Dordr.)* **55**, 543–554 (2013).
90. Gu, D., Andreev, K. & Dupre, E. M. Major Trends in Population Growth Around the World. *China CDC Wkly* **3**, 604–613 (2021).
91. Liu, Y. et al. Dynamical Madden–Julian Oscillation forecasts using an ensemble subseasonal-to-seasonal forecast system of the IAP-CAS model. *Geosci. Model Dev.* **17**, 6249–6275 (2024).
92. Neena, J. M., Lee, J. Y., Waliser, D., Wang, B. & Jiang, X. Predictability of the Madden–Julian Oscillation in the Intraseasonal Variability Hindcast Experiment (ISVHE)*. *J. Clim.* **27**, 4531–4543 (2014).
93. Bartana, H., Garfinkel, C. I., Shamir, O. & Rao, J. Projected future changes in equatorial wave spectrum in CMIP6. *Clim. Dyn.* **60**, 3277–3289 (2023).
94. Lin, Q., Mayta, V. C. & Adames Corraliza, Á. F. Assessment of the Madden-Julian Oscillation in CMIP6 Models Based on Moisture Mode Theory. *Geophys. Res. Lett.* **51**, e2023GL106693 (2024).
95. Jiang, X. et al. Fifty Years of Research on the Madden-Julian Oscillation: Recent Progress, Challenges, and Perspectives. *J. Geophys. Res. Atmos.* **125**, e2019JD030911 (2020).
96. Chang, C.-P. & Lim, H. Kelvin Wave-CISK: A Possible Mechanism for the 30–50 Day Oscillations. *J. Atmos. Sci.* **45**, 1709–1720 (1988).
97. Hendon, H. H. A Simple Model of the 40-50 Day Oscillation. *J. Atmos. Sci.* **45**, 569–584 (1988).
98. Wang, B. & Rui, H. Dynamics of the Coupled Moist Kelvin–Rossby Wave on an Equatorial β -Plane. *J. Atmos. Sci.* **47**, 397–413 (1990).
99. Hu, Q. & Randall, D. A. Low-Frequency Oscillations in Radiative-Convective Systems. *J. Atmos. Sci.* **51**, 1089–1099 (1994).
100. Yang, D. & Ingersoll, A. P. Triggered Convection, Gravity Waves, and the MJO: A Shallow-Water Model. *J. Atmos. Sci.* **70**, 2476–2486 (2013).
101. Hendon, H. H. & Salby, M. L. The Life Cycle of the Madden–Julian Oscillation. *J. Atmos. Sci.* **51**, 2225–2237 (1994).
102. Tian, B. et al. Vertical Moist Thermodynamic Structure and Spatial–Temporal Evolution of the MJO in AIRS Observations. *J. Atmos. Sci.* **63**, 2462–2485 (2006).
103. Wang, J., DeFlorio, M. J., Kim, H., Guirguis, K. & Gershunov, A. Future MJO Change and Its Impact on Extreme Precipitation and Temperature Over the Western US in CMIP6. *J. Geophys. Res. Atmos.* **130**, e2024JD042123 (2025).
104. Liebmann, B. & Smith, C. A. Description of a Complete (Interpolated) Outgoing Longwave Radiation Dataset. *Bull. Am. Meteorol. Soc.* **77**, 1275–1277 (1996).
105. Hersbach, H. et al. The ERA5 global reanalysis. *Q. J. R. Meteorological Soc.* **146**, 1999–2049 (2020).
106. Roberts, J. & Roberts, T. D. Use of the Butterworth low-pass filter for oceanographic data. *J. Geophys. Res. Oceans* **83**, 5510–5514 (1978).
107. Lloyd, S. Least squares quantization in PCM. *IEEE Trans. Inf. Theory* **28**, 129–137 (1982).
108. Arthur, D. & Vassilvitskii, S. k-means++: the advantages of careful seeding. in *Proceedings of the Eighteenth Annual ACM-SIAM*

Symposium on Discrete Algorithms 1027–1035 (Society for Industrial and Applied Mathematics, New Orleans, Louisiana, 2007).
109. Sen, P. K. Estimates of the Regression Coefficient Based on Kendall's Tau. *J. Am. Stat. Assoc.* **63**, 1379–1389 (1968).
110. Mann, H. B. Nonparametric Tests Against Trend. *Econometrica* **13**, 245 (1945).
111. Kendall, M. G. *Rank Correlation Methods* (Griffin, London, 1975).
112. Gilbert, R. O. *Statistical Methods for Environmental Pollution Monitoring* (Wiley, 1987).
113. Eyring, V. et al. Overview of the Coupled Model Intercomparison Project Phase 6 (CMIP6) experimental design and organization. *Geosci. Model Dev.* **9**, 1937–1958 (2016).
114. Pawlowicz, R. M._Map: A Mapping package for Matlab (Version 1.4 m) [Software]. http://www.eoas.ubc.ca/~rich/map.html (2020).

Acknowledgements

This work was supported by National Key Research and Development Program of China grant (2024YFF0809200 to F.L.), the National Science Foundation/Climate Dynamics Award (#2025027 to B.W.), the Hong Kong Research Grant Council (RGC) Postdoctoral Fellowship Scheme 2023/24 (PDFS2324-6S05 to T.F.C), General Research Fund (16300424 to M.L.), Collaborative Research Fund (C6032-21G to M.L.), and the Theme-based Research Scheme (T22-501/23-R to M.L.). T.F.C. and M.L acknowledge the support from the Otto Poon Centre for Climate Resilience and Sustainability at HKUST. The authors acknowledge the Working Group on Coupled Modelling (WGCM) under the World Climate Research Programme (WCRP) and the climate modeling groups for making the CMIP6 model outputs available.

Author contributions

T.F.C. contributed to the methodology, investigation, visualization, original draft, and manuscript revision. B.W. contributed to the conceptualization, methodology, investigation, project supervision, and manuscript revision. F.L. contributed to the investigation and manuscript revision. G.C. contributed to the method and manuscript revision. M.L. contributed to the manuscript revision. All co-authors contributed to the discussion of the results.

Competing interests

The authors declare no competing interests.

Additional information

Supplementary information The online version contains supplementary material available at https://doi.org/10.1038/s41467-025-58955-4.

Correspondence and requests for materials should be addressed to Bin Wang or Fei Liu.

Peer review information *Nature Communications* thanks Victor Mayta and the other, anonymous, reviewer for their contribution to the peer review of this work. A peer review file is available.